CHALMERS
UNIVERSITY OF TECHNOLOGY

# Boosting Second-Harmonic Generation in Monolayer Rhenium Disulfide by Reversible Laser Patterning

Downloaded from: https://research.chalmers.se, 2025-12-05 01:46 UTC

Citation for the original published paper (version of record):
Kücüköz, B., Munkhbat, B., Shegai, T. (2022). Boosting Second-Harmonic Generation in Monolayer Rhenium Disulfide by Reversible Laser
Patterning. ACS Photonics, 9(2): 518-526. http://dx.doi.org/10.1021/acsphotonics.1c01358

N.B. When citing this work, cite the original published paper.

research.chalmers.se offers the possibility of retrieving research publications produced at Chalmers University of Technology. It covers all kind of research output: articles, dissertations, conference papers, reports etc. since 2004. research.chalmers.se is administrated and maintained by Chalmers Library

(article starts on next page)

ACS Photonics

pubs.acs.org/journal/apchd5 Article

# Boosting Second-Harmonic Generation in Monolayer Rhenium Disulfide by Reversible Laser Patterning

Betül Küçüköz, Battulga Munkhbat, and Timur O. Shegai*

Cite This: *ACS Photonics* 2022, 9, 518−526 Read Online

ACCESS | Metrics & More | Article Recommendations | Supporting Information

**ABSTRACT:** Active modification and control of transition metal dichalcogenides (TMDs) properties are highly desirable for next-generation optoelectronic applications. In particular, controlling one of the most important characteristics of TMDs—their crystal structure and symmetry—may open means for manipulating their optical nonlinearities and electrical transport properties. Here, we show that a monolayer $ReS_2$, which does not have a broken inversion symmetry due to its stable 1T′-distorted phase and correspondingly shows only weak second-harmonic generation (SHG), can produce a significantly enhanced (∼2 orders of magnitude) SHG upon reversible laser patterning. This enhancement can be explained by the laser-induced transition from centrosymmetric 1T′ to noncentrosymmetric 2H-phase. This hypothesis is confirmed by polarization-resolved SHG measurements, which reveal a gradual change from the 2-fold to 6-fold symmetry profiles upon laser patterning. Additionally, we found that laser patterning of the bilayer $ReS_2$ samples, contrary to the monolayers, leads to a substantially reduced SHG signal. This result corroborates the 1T′-to-2H laser-induced phase transition. Finally, we show that the laser-induced patterning is reversible by heat. These results open a possibility to actively and reversibly control the crystal structure of mono- and few-layer $ReS_2$ and thus its optical and electronic properties.

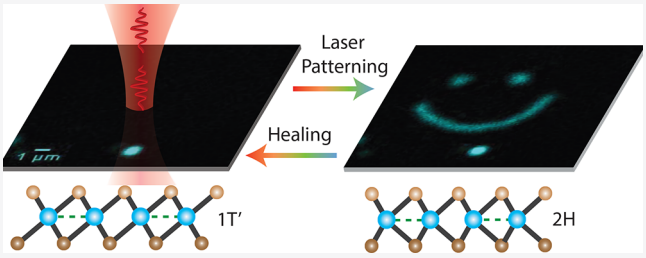


**KEYWORDS:** *$ReS_2$, second-harmonic generation, laser-induced patterning, phase transition*

Downloaded via 155.4.234.165 on March 7, 2022 at 13:11:23 (UTC).
See https://pubs.acs.org/sharingguidelines for options on how to legitimately share published articles.

## ■ INTRODUCTION

Crystal structure and symmetry play an important role in determining key material properties, such as the electrical transport behavior and the level of optical nonlinearities.[1−4] Many group VI transition metal dichalcogenides (TMDs), including $MoS_2$, $WS_2$, and $WSe_2$, follow the 2H crystalline structure in their most stable configuration and thus possess a broken inversion symmetry in the monolayer form. This leads to a pronounced second-harmonic generation (SHG) signal due to the high second-order susceptibility, $\chi^{(2)}$.[5−7] In fact, the values of $\chi^{(2)}$ nonlinear coefficient for monolayer $MoS_2$ are among the highest reported to date—up to $10^{-7}$ m/V at 810 nm excitation.[6,8] Therefore, significant research attention is devoted to studying these nonlinear optical effects.[9−13]

One way to boost the optical nonlinearity in symmetric structures, such as multilayer $WS_2$ and alike, is through using the edges of TMD materials, where the inversion symmetry is broken, either naturally[14] or artificially.[15,16] Additionally, strain can be used to break the inversion symmetry and thus to enhance the SHG.[17,18] In a similar manner, strain can be used to enhance the SHG from symmetric TMD structures.[19−22] Moreover, the even order optical nonlinearity, mechanical stress, and broken inversion symmetry in monolayer TMDs are inherently related to the piezoelectric effect, which has been recently reported for $MoS_2$.[3,23]

Contrary to the common Mo- and W-containing dichalcogenides, a monolayer $ReS_2$ has a different stable crystallographic phase, 1T′-distorted, which is centrosymmetric.[24] Thus, no substantial SHG is expected to originate from a monolayer $ReS_2$.[24] Since Re atoms have additional valence electrons, they form strong covalent bonds between the neighboring Re atoms. The Re−Re chains cause the distortion of the crystal structure and thereby provide a distinguished in-plane anisotropy of the $ReS_2$ crystal. This unique in-plane distortion makes the multilayer $ReS_2$ more complicated than many other TMD materials with no distortion. This complexity affects the interlayer coupling and stacking. Several previous studies demonstrated that $ReS_2$ has a weak interlayer coupling and a randomly stacked geometry due to in-plane distortion.[25−29] In contrast, several other studies claimed the layers are coupled and stacked in an orderly fashion as evidenced by the appearance of interlayer shear and breathing modes measured by ultralow frequency Raman spectrosco-

**Received:** September 7, 2021
**Published:** January 24, 2022

ACS Publications © 2022 The Authors. Published by American Chemical Society



https://doi.org/10.1021/acsphotonics.1c01358
*ACS Photonics* 2022, 9, 518−526

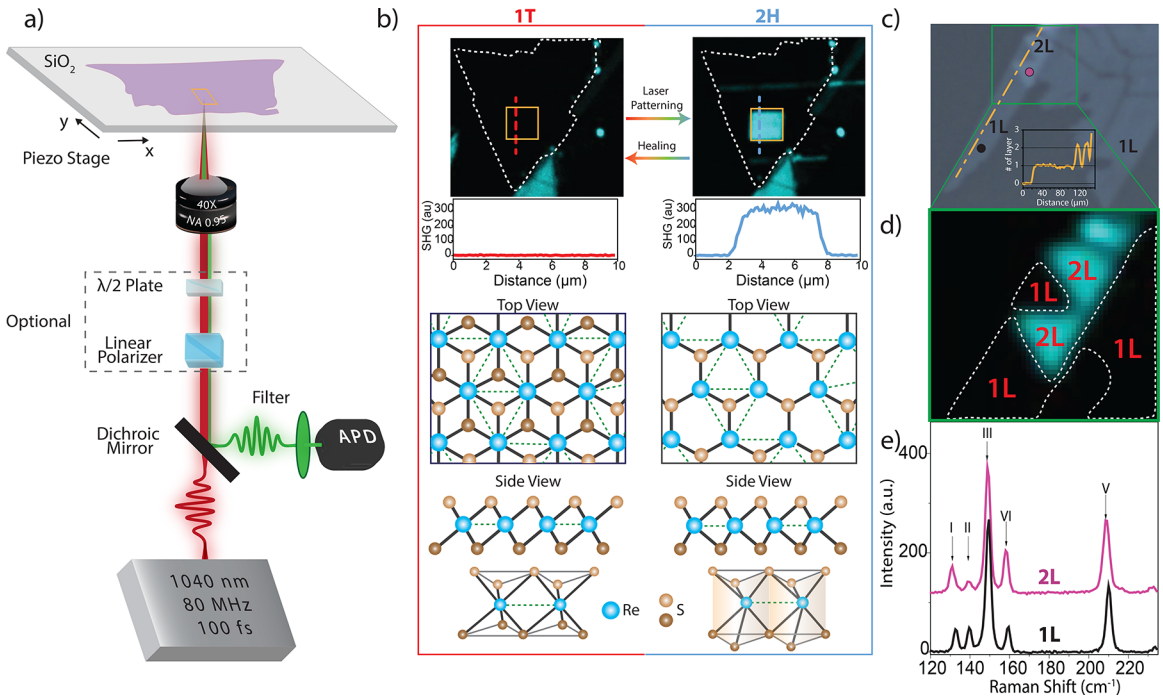


**Figure 1.** (a) Schematic diagram of the experimental setup for SHG measurements and laser patterning. (b) Spatial SHG map of an unpatterned monolayer $ReS_2$ marked with a white dotted line and an SHG intensity profile analyzed along the dashed line (left, top) and a laser-patterned monolayer (marked with an orange box) and analyzed SHG intensity profile of the patterned area (right, top). A substantial (∼2 orders of magnitude) enhancement of the SHG is observed for the laser-patterned monolayer. All SHG images are presented in false color. (bottom) Crystalline structure of the 1T (left) and 2H phases (right). Green dashed lines schematically illustrate formation of Re−Re bonds in $ReS_2$. (c) Optical microscope image of the mono- and bilayer $ReS_2$. (inset) Gray scale contrast profile relative to the substrate along the dashed−dotted line profile. (d) SHG spatial map of the unpatterned mono- and bilayer $ReS_2$ on a glass substrate. Notice a considerably higher SHG signal from the bilayer region. (e) Raman spectra of $ReS_2$ mono- and bilayer measured at the positions marked with black and pink circles in c, respectively. $A_g$-like and $E_g$-like Raman modes are labeled as I and III, respectively.

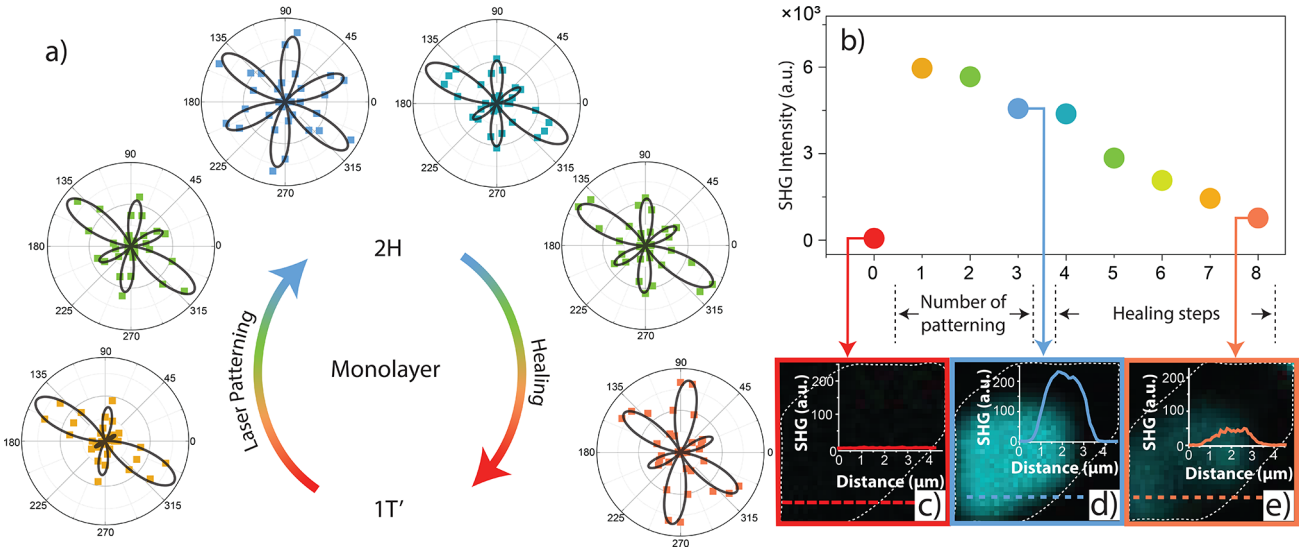


**Figure 2.** (a) Polarization-resolved SHG intensity for laser patterning and spontaneous healing steps that show reversible phase transition from 1T′ to 2H. Filled squares show the experimental data, and solid lines represent theoretical fits using eq 2 in the polar plots. The *b*-axis of the $ReS_2$ crystal is aligned to the *y*-axis of the polar plots at $\theta_0 = 0$. The experimental data was normalized by its maximum value. (b) Integrated SHG intensity as a function of a number of patterning and healing steps for the $ReS_2$ monolayer, obtained from data in a. (c−e) SHG spatial maps (recorded without a polarizer and a $\lambda/2$ plate) of unpatterned (c), laser-patterned (d), and healed (e) monolayer $ReS_2$, respectively. The SHG intensity was analyzed along the dashed line (the monolayer is marked with white dotted lines).

py.[30−33] Furthermore, each stacking order (AA and AB) has different optical properties and carrier dynamics.[34]

To date, only a few studies reported SHG from mono- and multilayers of $ReS_2$. Specifically, Song et al.[24] observed that the SHG signal is strongly dependent on the number of layers in a few-layer $ReS_2$ sample. The even number of layers was reported to provide a much stronger SHG signal than the odd number of layers, due to the broken inversion symmetry of the


https://doi.org/10.1021/acsphotonics.1c01358
ACS Photonics 2022, 9, 518−526

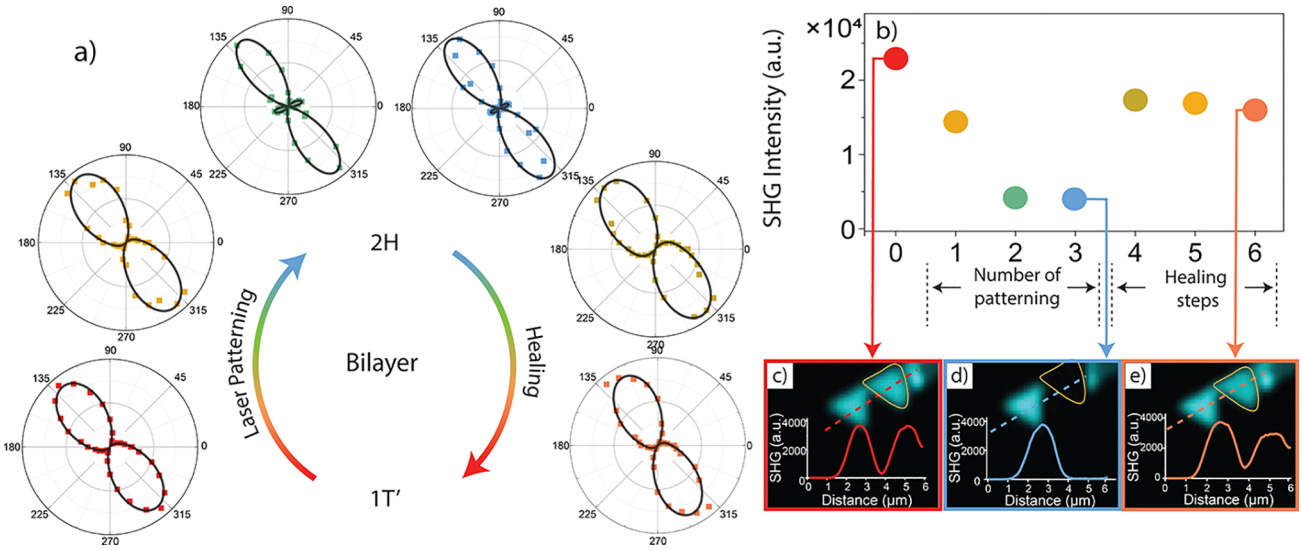


**Figure 3.** (a) Polarization-resolved SHG intensity for laser patterning and spontaneous healing steps that shows reversible phase transition from 1T′ to 2H. Filled squares show the experimental data, and solid lines represent theoretical fits using eq 2 in the polar plots. The *b*-axis of the $ReS_2$ crystal is aligned to the *y*-axis of the polar plots at $\theta_0 = 0$. The experimental data was normalized by its maximum value. (b) Integrated SHG intensity as a function of a number of patterning and healing steps for the $ReS_2$ bilayer, obtained from data in a. (c−e) SHG spatial mapping images (recorded without a polarizer and a $\lambda/2$ plate) of unpatterned (c), laser-patterned (d), and healed (e) bilayer $ReS_2$, respectively, and the SHG intensity is analyzed along the dash line (the laser-patterned bilayer is marked by orange lines).

corresponding multilayers.[24] Contrary to that, Dhakal et al. reported no evident even−odd number effect but instead observed a monotonic increase of the SHG signal with increasing number of layers.[35] However, none of these works reported a reversible laser-induced phase changes in $ReS_2$ as we study here.

Laser-induced modifications of a TMD crystal structure and topology were reported previously, especially in relation to $MoTe_2$[36−39] and $MoS_2$.[40] However, these changes were not reversible, because of the permanent damage of the material through layer-by-layer laser ablation.[36−39] Additionally, a modification of TMDs crystal structure can be achieved by chemical means, for instance, by electron donation from lithium during intercalation when it is exposed to *n*-butyl lithium.[41−44]

Here, we show that mono- and bilayer $ReS_2$ can experience reversible laser-induced crystal structure changes as evidenced by the substantial boosting (∼2 orders of magnitude) or reduction (also ∼2 orders of magnitude) of the SHG signal, respectively (see Figure 1b). These changes can be explained by transition from the 1T′-distorted to 2H-phase, which is confirmed both by the strength of the SHG signal and the polarization analysis of the SHG emission. These findings open new possibilities for active control of the crystal structure of 2D materials and their heterostructures and therefore their optical and electronic properties. As an outlook, we envision a reversible metal-to-insulator transition induced by this process.

## ■ RESULTS AND DISCUSSION

In our experiments, two different types of SHG detection was used: (i) total and (ii) polarization-resolved. In both cases, the samples were excited by a linearly polarized 1040 nm laser beam. The difference between the measurements was that in case ii the excitation and detection were performed through a linear polarizer and installed between the objective and the dichroic mirror; moreover, a half-wave ($\lambda/2$) plate was additionally installed in order to rotate the polarization of the incident laser beam with respect to the $ReS_2$ flake. In case i, neither the $\lambda/2$ plate nor the polarizer was used. The first type of detection was used in experiments shown in, e.g., Figure 1b,d, while the second type was used in experiments shown in Figures 2a,b and 3a,b. We thus separate the discussion of the results into two parts, in accordance with the measurement type.

**Total SHG Intensity Measurements.** We start with a monolayer $ReS_2$ flake illuminated by a femtosecond laser beam at a wavelength of 1040 nm. The SHG signal is collected at 520 nm, as shown in Figure 1a (see Methods for details of sample preparation). To prove the signal is indeed due to SHG, we performed several laser power-dependent measurements and obtained a slope ∼2 in the log−log scaled SHG intensity vs laser power plot (Figure S1). Furthermore, we observed almost no SHG signal from the monolayer $ReS_2$, but a significant SHG could be seen from the bilayer $ReS_2$ located nearby (Figure 1d). We interpret this as being due to the centrosymmetric and noncentrosymmetric crystal structure of the monolayer and bilayer, respectively (Figure 1b−d). This even−odd number effect is consistent with observations of Song et al.[24]

Despite the fact the monolayer $ReS_2$ showed only a very weak SHG signal initially, we observed that by exposing it to a femtosecond laser beam at an elevated laser intensity and for an extended period of time (see Methods), the SHG intensity can be boosted nearly 2 orders of magnitude (see top panel in Figure 1b). Such an increase in the SHG signal may be attributed to a change in the crystal structure of the $ReS_2$ monolayer−from the initial centrosymmetric structure to the one with the broken inversion symmetry after the laser exposure. A specific example of such a crystal structure change could be a transition from the centrosymmetric 1T′ phase to noncentrosymmetric 2H-phase (Figure 1b). For simplicity of visualization, in Figure 1b, the phase transition is illustrated as if it was occurring from the undistorted 1T′ to 2H phase (instead of the more realistic distorted 1T′, which is the stable


https://doi.org/10.1021/acsphotonics.1c01358
ACS Photonics 2022, 9, 518−526

phase of $ReS_2$). The formation of Re−Re bonds due to the extra valence electrons of the Re atoms is schematically shown by dashed green lines in the crystal structure.

Optical image of the mechanically exfoliated mono- and bilayer $ReS_2$ flakes on a glass substrate is shown in Figure 1c and a corresponding SHG spatial map in Figure 1d. The inset in Figure 1c presents the profile analysis of the gray scale contrast of the flakes with respect to the substrate. This data offers a simple means to determine the thickness through optical contrast. The mono- and bilayer nature of the $ReS_2$ flakes was further confirmed by Raman spectroscopy, Figure 1e.[26] In Raman spectra, the peak position differences between an $E_g$-like mode (III) and an $A_g$-like mode (I) are increasing with the increasing number of layers, which is consistent with the AB-stacked (anisotropically stacked) $ReS_2$.[30] Furthermore, the anisotropic stacking has a broken inversion symmetry for even number of layers and hence should be SHG-active, which agrees with our SHG data for the bilayer (see Figure 1d). An alternative AA-(isotropic) stacking of $ReS_2$ has an inversion symmetry for an even number of layers and hence should be SHG-inactive. This regime is not observed in our samples, for which reason we conclude that we deal with the AB-(anisotropically) stacked 1T′-distorted phase of $ReS_2$.

**Polarization-Resolved Measurements.** The SHG spectroscopy is an efficient way to investigate the crystalline structure of a material since it features strong polarization dependence with small alterations in the atomic lattice. To investigate the reversible phase changes by laser patterning, polarization-resolved SHG measurements were performed for both mono- and bilayer $ReS_2$ (additional Raman spectra for unpatterned and laser-patterned $ReS_2$ monolayers are shown in the SI Figure S2). This was done by rotating the $\lambda/2$ plate installed in front of the objective lens as shown in Figure 1a. The optical setup allows us to control the polarization of the incident laser beam (1040 nm) and collect the SHG signal (520 nm) in reflection mode through the same $\lambda/2$ plate and polarizer (with polarization parallel to the incident laser beam). In all polarization-resolved SHG measurements, only the parallel-polarized SHG was collected ($I_{SHG}^{\parallel}$). The angle-averaged polarization-resolved SHG signal (Figures 2b and 3b) was obtained by integrating the corresponding polarization-dependent plots (Figures 2a and 3a) over all polarization directions, which ensures averaging out any orientation-related effects.

Polarization-resolved SHG measurements provide invaluable information, which is directly linked to the crystalline structure of the flake. In our case, the polarization-resolved data indicates a laser-induced modification of the crystalline structure of $ReS_2$ monolayer (Figure 2a). At first, the SHG measurement was performed on an unpatterned monolayer in polarization-resolved (Figure 2a) and subsequently integrated SHG intensity manner (Figure 2b). It was reported previously that a monolayer $ReS_2$ is centrosymmetric and hence SHG inactive.[24] Thus, the polar plot for the unpatterned monolayer could not be obtained (nearly no signal detected). Second, the flake was exposed to the focused 1040 nm laser beam at an elevated (0.8 mW) power. The patterning was performed in a step-like manner by scanning the beam across the sample at a rate of 50 nm/step using a piezo stage (the beam diameter was ∼1 $\mu$m, each step was approximately 50 nm—much smaller than the beam diameter). At each patterning step, the beam was parked at a certain location for 200 ms. Overlapping of the sequential patterning steps allows to induce a phase transition over a predefined area in a homogeneous manner. The patterning parameters were optimized to ensure no permanent damage of the sample. After each patterning of a predefined area, a polarization-resolved SHG measurement (at low laser power) was performed (from that predefined area) to continuously monitor the phase transition behavior (see Figure 1a). The details of measurements and analysis are given in the Supporting Information (Figure S3).

In our measurements, a gradual evolution of polar plots from 2-fold-like to 6-fold-like symmetry profiles is observed (Figure 2a). After a three-time repetitive patterning of the same area, a nearly perfect 6-fold symmetry profile was obtained, which is the characteristic polarization profile of the 2H-phase. These results show that (i) a phase modification of the monolayer $ReS_2$ is possible by laser patterning and (ii) more interestingly such patterning can boost the SHG intensity due to the centrosymmetric to noncentrosymmetric structure transition.

A similar phase transition was previously observed for multilayers of $MoTe_2$ upon laser irradiation,[36−39] however, in these studies the patterning was based on an irreversible process—a laser ablation of a top layer(s) in a multilayer flake. Previously, a polarization-dependent SHG intensity variation collected from a monolayer $ReS_2$ has been also reported.[35] The signal exhibited a butterfly like pattern in the polar plots, similar to our observations in healing steps (Figure 2a).

In order to demonstrate that the phase transition is reversible in our case, the samples have been left undisturbed in dark at room temperature for several days. This resulted in spontaneous "healing" of the sample, which was also monitored by polarization-resolved SHG measurements (Figure 2a) and by integrated SHG intensity changes (Figure 2b). The recovery of the 1T′-phase pattern in the polar plots and the integral SHG intensity reduction prove that the phase of the patterned $ReS_2$ changes back from the 2H to the more stable 1T′. Although this recovery process was rather slow at room temperature (the process took several days, Figure 2), it could be significantly accelerated by heating (see Figure S4).

Similar to the monolayer, we have also studied the effect of laser patterning on the phase modification of a bilayer $ReS_2$. As mentioned above, the unpatterned bilayer has a non-centrosymmetric structure (for AB stacking). Thus, it showed an intense SHG signal (Figure 1d), which followed a 2-fold symmetry in its polarization-resolved profile as expected for the 1T′-phase (Figure 3a).[24,38] The maximum SHG intensity was obtained when the incident light was polarized parallel to the *b*-axis of the crystal, which corresponds to the distortion along the Re−Re chain (Figure 3a). By applying the same laser patterning procedure as for the monolayer case, the bilayer $ReS_2$ can also be patterned. Unlike the monolayer case, however, the SHG intensity of the laser-patterned bilayer *decreased* significantly (∼2 orders of magnitude) (Figure 3b,d). We performed three patterning steps and recorded the corresponding polarization-resolved SHG data in each step. The reduction of the SHG signal implies the phase modification toward the centrosymmetric structure, which could be a 2H-phase of an AB-stacked bilayer. This hypothesis is in agreement with the 1T′-to-2H transition of the monolayer discussed in Figure 2. The reversibility of the phase transition was also monitored systematically by the polarization-resolved SHG measurements. It is worth mentioning that the spontaneous healing of the bilayer (back to the 1T′ phase) is much faster than for the monolayer $ReS_2$. While the monolayer healing took several days at room temperature, it


https://doi.org/10.1021/acsphotonics.1c01358
ACS Photonics 2022, 9, 518−526

took just a few hours for the bilayer $ReS_2$. However, it is also worth mentioning that the healing of both the patterned mono- and bilayer $ReS_2$ did not result in a full recovery. Instead, only about 85% recovery (counted as total SHG signal) was observed during the spontaneous healing process at room temperature (Figures 2e and 3e). Heating the samples can speed up the recovery and, additionally, lead to the recovery of as much as ∼95% of the original SHG signal. This result was obtained by a three-step heating of the laser-patterned $ReS_2$ flake with different temperatures 100, 150, and 200 °C (an hour for each step) (Figure S4).

**Analysis of the Nonlinear Tensors.** Next, we analyze the $\chi^{(2)}_{ijk}$ nonlinear tensor components. This is done by fitting the measured polarization-dependent SHG intensity for each laser patterning and healing steps for both mono- and bilayer $ReS_2$ flakes. It is important to confirm the occurrence of crystal structure modification by studying the relative changes of the $\chi^{(2)}$ tensors, as these are directly related to the crystalline structure and its symmetry. Therefore, the expected laser-induced 1T′-to-2H phase transition should be directly seen in variation of the $\chi^{(2)}$ tensor component(s), which can be monitored by polarization-resolved SHG.

In our further analysis, we set $x$ and $y$ axes to lie in-plane, while $z$ axis perpendicular to the plane of the flake. Furthermore, for simplicity we neglect any out-of-plane contributions to the nonlinear polarization.[24] The SHG intensity for a certain in-plane orientation of the incident linear polarization with respect to the principal axis of the second-order nonlinear tensor (given by angle $\theta$) is expressed in terms of $\chi^{(2)}$-tensor components and trigonometric functions of $\theta$. The general expression is rather complicated, but it can be substantially simplified, assuming the Kleinman's symmetry conditions: $\chi^{(2)}_{xxy} = \chi^{(2)}_{xyx} = \chi^{(2)}_{yxx}$ and $\chi^{(2)}_{xyy} = \chi^{(2)}_{yxy} = \chi^{(2)}_{yyx}$. Kleinman's symmetry is assumed when the excitation frequency is smaller than the lowest absorption frequency of the material,[45] implying it could be applicable in our case, since the excitation wavelength (1040 nm) is longer than the A-exciton resonance wavelength of $ReS_2$ (∼800 nm).

The total SHG intensity is given as a sum of ⊥ and ∥ channels, with orientations determined with respect to the original laser polarization: $I^{tot}_{SHG}(\theta) = I^{\perp}_{SHG}(\theta) + I^{\parallel}_{SHG}(\theta)$ . This expression for the total SHG intensity can be used to describe our observations in Figure 1. The corresponding intensity components are given by

$$I^{\perp}_{SHG}(\theta) = |-\chi^{(2)}_{xxx}\cos^2\theta\sin\theta + \chi^{(2)}_{xxy}(\cos^3\theta - \sin 2\theta\sin\theta) + \chi^{(2)}_{xyy}(\cos\theta\sin 2\theta - \sin^3\theta) + \chi^{(2)}_{yyy}\cos\theta\sin^2\theta|^2 \quad (1)$$

and

$$I^{\parallel}_{SHG}(\theta) = |\chi^{(2)}_{xxx}\cos^3\theta + 3\chi^{(2)}_{xxy}\cos^2\theta\sin\theta + 3\chi^{(2)}_{xyy}\cos\theta\sin^2\theta + \chi^{(2)}_{yyy}\sin^3\theta|^2 \quad (2)$$

Note that the polarization-resolved SHG intensities, recorded in Figures 2a and 3a, were fitted by eq 2. The fits are shown as continuous lines in both figures and are in good agreement with the experimental data. The corresponding $\chi^{(2)}$ tensor components and their evolution with patterning and healing steps are shown in the SI (see Supplementary Tables S1 and S2 and Figure S5) for both the $ReS_2$ mono- and bilayer. Overall, the tensor components systematically follow pattering and healing steps and reproduce the polarization-resolved profiles for both monolayer and bilayer cases. Additional details about the fitting procedure are provided in the SI. Additional examples of polarization-resolved experiments, which reproduce the observations in Figures 2 and 3 are shown in Figures S6 and S7 for the mono- and bilayer cases, respectively.

Notice that upon imposing additional symmetry requirements on the tensor components, such as $\chi^{(2)}_{xxx} = \chi^{(2)}_{xyy} = 0$ and $\chi^{(2)}_{yyy} = -\chi^{(2)}_{xxy}$, which hold for the $D_{3h}$ symmetry,[38,45,46] we obtain a 6-fold polar plot, that is typical for 2H-phase TMD monolayers:

$$I^{\parallel}_{SHG}(\theta) \propto \sin^2 3\theta \quad (3)$$

A similar 6-fold-like polar plot was observed experimentally in Figure 2a, after three patterning steps, confirming that laser-induced patterning of the monolayer $ReS_2$ leads to a 1T′-to-2H transition. This observation also speaks against alternative scenarios of SHG enhancement, for example, related to laser-induced stress (e.g., bubble formation and deposition of impurities) or photodamage of the substrate.

We note that in all equations above, one should additionally consider an unknown orientation of the laboratory frame with respect to the $ReS_2$ crystal frame. In the fits this was done by exchanging: $\theta \to \theta - \theta_0$, where $\theta_0$ is this unknown orientation. It is important to mention that the fits for both mono- and bilayer samples resulted in nearly identical values of $\theta_0 \approx 55 \pm 3°$, which agrees with the fact that both mono- and bilayer samples were exfoliated from the same $ReS_2$ flake. This result further validates our fitting procedure.

Finally, we would like to note that the total SHG intensity, $I^{tot}_{SHG}(\theta)$, described by the sum of eq 1 and 2, should be able to match the ∼2 orders of magnitude boosting (reduction) in the SHG signal upon laser patterning of monolayer (bilayer) samples. These data are shown in Figures 2c−e and 3c−e for monolayer and bilayer cases, respectively. The integrated $I^{\parallel}_{SHG}$ shown in Figures 2b and 3b, however, shows a smaller level of boosting and reduction than the unpolarized data. This is especially evident for the bilayer case (compare Figure 3b with c−e). In an attempt to explain this discrepancy, in Figure S8 we plot a simulated angle-dependent $I^{\parallel}_{SHG}(\theta)$ and $I^{\perp}_{SHG}(\theta)$, as well as $I^{tot}_{SHG}(\theta)$ with typical $\chi^{(2)}$ parameters extracted from the polarization-resolved fits. These plots allow estimation of the relative difference between $I^{\parallel}_{SHG}(\theta)$ and $I^{tot}_{SHG}(\theta)$, despite the fact that $I^{\perp}_{SHG}(\theta)$ was not measured in our experiments. The results are such that for the monolayer case the angle-averaged $I^{\parallel}_{SHG}$ is on the order of 1/2 of $I^{tot}_{SHG}$, while for the bilayer case the polarized and total signals are almost the same. This implies that the discrepancy between the total and polarization-resolved signal cannot be explained solely by the use of polarization optics. Instead, a possible explanation could involve contributions from out-of-plane, $z$, $\chi^{(2)}$ tensor components, which we have ignored in this analysis for the sake of simplicity. Since in experiments we used an 40× NA = 0.95 air objective, the contribution of the out-of-plane tensor components to the SHG signal might be non-negligible. However, a quantitative account of this possibility goes outside of the scope of this study.

**Mechanism of Laser-Induced Crystal Structure Modification.** To shed light on the mechanism behind the laser-


https://doi.org/10.1021/acsphotonics.1c01358
ACS Photonics 2022, 9, 518−526

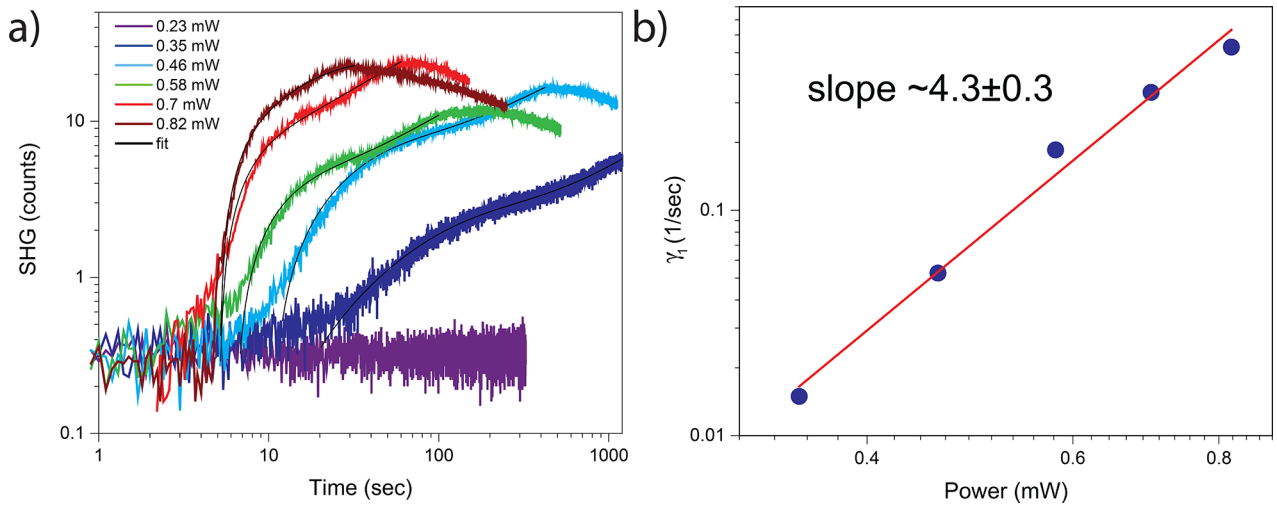


**Figure 4.** (a) Time evolution of the SHG signal intensity of monolayer $ReS_2$ with different excitation power at 1040 nm in log−log scale. The signal at each laser power was collected by parking a focused laser beam at a certain location on the flake and monitoring the SHG($t$), as the 1T′-to-2H phase transition proceeds. Several laser intensities were used at different locations of the same monolayer flake to monitor the power dependence of the patterning process. (b) Log−log plot of the SHG growth rate vs laser power, showing the slope of 4.3 ± 0.3, which indicates a highly nonlinear origin of the transition. Error bars are smaller than the symbol size.

induced reversible phase transition, we performed several control experiments. Our general hypothesis was that the laser-induced changes can be either due to nonequilibrium thermal effects or photoinduced. We note that *no* change in a crystal structure in either a monolayer or bilayer $ReS_2$ could be initiated by a homogeneous (adiabatic) heating of the samples by a hot plate. This suggests that if the laser-induced crystal structure modification is due to a thermal effect, then this thermal effect must be nonhomogeneous and nonadiabatic. Moreover, we note that in a net result *no* reversed 2H-to-1T′ crystal structure change could be induced by the laser (although the laser contribution to the reversed process is hard to isolate with certainty, since the laser may have two effects—electronic excitation and nonequilibrium heating). This observation implies that the hypothetical nonadiabatic thermal effect is only able to switch the crystal structure in the direction of 1T′ → 2H, but not in the reversed 2H → 1T′ direction. Such a unidirectional laser-induced crystal structure change can also be consistently explained by a photochemical process involving an asymmetric excited state, which is typical for photoisomerization of organic molecules.[47,48]

Since several earlier studies mainly focused on thermal effects in multilayer $MoTe_2$,[36−39] we verified the role of a substrate in the patterning process. Specifically, we used a Si/$SiO_2$ substrate to increase the heat dissipation. These experiments showed that the monolayer patterning on the Si/$SiO_2$ substrate was possible but it required higher laser powers and longer exposure times to modify the crystal structure (see Figure S9). Since silicon substrates generally have a higher heat dissipation than glass, these experiments indicate that the laser-induced phase modification might be due to a nonadiabatic thermal process (however, as we show below, a photoinduced scenario is more likely).

In addition to thermal conductivity, the role of a substrate can be in providing different roughness and $ReS_2$ adhesion conditions. Thus, the atomic displacement required for the phase change can be potentially inhibited or sped up, depending on the substrate. Leftovers of a polydimethylsiloxane (PDMS) stamp used for the flake transfer can also affect the switching process. These effects are common for both thermal and photophysical routes.

To elucidate the power-dependent nature of the laser patterning process, we recorded a series of time-dependent SHG($t$) signals as the focused laser beam was parked at a certain position on the monolayer. The laser power was adjusted such that we could both induce phase transition and record SHG signal simultaneously. This procedure was repeated several times with increasing laser power, each time starting from a fresh unpatterned region of the monolayer. This data is shown in Figure 4. We fit the observed SHG($t$) to an exponential growth function and analyzed the resulting time-constants ($\gamma$) as a function of laser power. The resulting enhancement rate showed a nearly 4-power dependence on the laser intensity, suggesting that the process is highly nonlinear and a multiple photon absorption is responsible for the observed 1T′-to-2H phase transition in monolayer $ReS_2$. This observation is supported by the fact that the linear absorption of $ReS_2$ in the 1040 nm spectral range is low (since the energy of a laser photon is below $ReS_2$ bandgap). The remarkable nonlinearity of the laser-induced process suggests that on the one hand, the 2H-phase regions might be localized to subdiffraction spots within any diffraction limited 1040 nm laser spots, and on the other, that a UV light would be able to switch the crystalline phase of $ReS_2$ in a more linear fashion, that is, without a need for intense femtosecond laser pulses. The latter additionally rules out the nonadiabatic heating scenario. To verify this hypothesis, we exposed a $ReS_2$ monolayer on a glass substrate to a broadband LED source combined with a long-pass filter, such that wavelengths below 488 nm were reflected toward the sample and focused on it by a 20× (NA = 0.45) objective. The power at the sample was 170 mW. The illumination wavelength range was restricted to ∼400−488 nm, and the integrated power was measured over the entire spectral range right after the microscope objective. After 6.5 h of illumination, the SHG spatial mapping has been performed again and a substantial increase in the SHG signal intensity was observed. The data is shown in Figure S10. These


https://doi.org/10.1021/acsphotonics.1c01358
ACS Photonics 2022, 9, 518−526

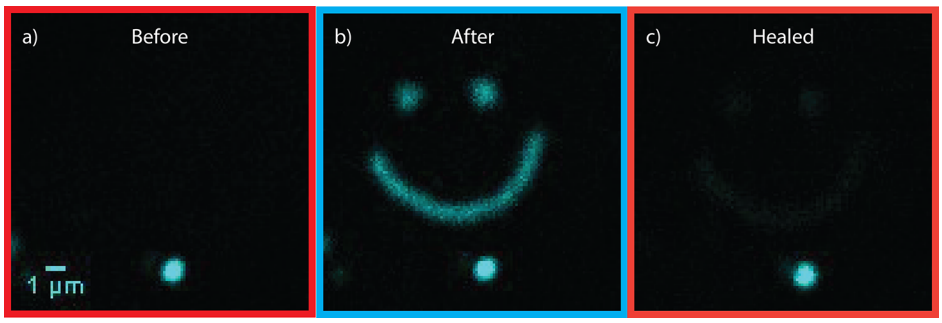


**Figure 5.** (a) SHG image of unpatterned monolayer $ReS_2$ flake. (b) Smiley face created by boosting the SHG signal using laser patterning. (c) "Erased" image on the same monolayer $ReS_2$, recorded after several days of spontaneous healing at room temperature. Images a−c were obtained under the same experimental conditions, and thus, the SHG intensities can be directly compared.

observations provide further evidence for the photoinduced nature of the observed 1T′-to-2H transition.

We note that a physical damage or permanent chemical bond breaking is unlikely during the crystal structure modification in our experiments (as is evident from the reversible nature of these changes). Thus, the laser-induced patterning can be safely applied to a few layer of $ReS_2$. To achieve a similar patterning of thicker multilayer flakes, however, either a higher laser power or longer exposure times are needed, as modifications of all layers are required. Such an increased laser power or exposure time may potentially lead to a permanent damage of the layer(s) in a multilayer $ReS_2$ structure, as was observed in $MoTe_2$ multilayer systems previously.[36−39] To avoid this problem, we have limited ourselves to experiments with mono- and bilayers of $ReS_2$ in this work.

A highly nonlinear reversible phase transition of $ReS_2$ monolayers and bilayers discussed here can be of potential interest for future applications. One possibility that we explored further was "writing" the SHG-encoded information by laser patterning and subsequently erasing this information by either a spontaneous healing or adiabatic heating. By using a piezo stage, we can control the position of the $ReS_2$ flake with respect to the focused laser beam (diameter ∼1 μm) with a subwavelength precision. To exemplify this process, we encoded a prototypical image—a smiley face—and "wrote" it by laser-induced patterning on the monolayer $ReS_2$. This enhanced the SHG signal from the monolayer only in the exposed areas, producing the SHG contrast due to the 1T′-to-2H phase transition (see Figure 5). The image can be subsequently erased by spontaneous healing or adiabatic heating due to reversed 2H-to-1T′ transition. This type of writing and erasing procedure can be applied multiple times to the same samples both in monolayer and bilayer forms. Such laser-induced patterning can be of potential interest not only for monolayer/bilayer $ReS_2$ but also for van der Waals heterostructures of this material with other members of the TMD family and beyond.

## CONCLUSION

In summary, we have studied a reversible laser-induced phase transition from 1T′-distorted to 2H phase for the mono- and bilayer $ReS_2$. Since the $ReS_2$ monolayer is centrosymmetric, the observed SHG intensity was very low. However, the SHG can be significantly boosted (∼2 orders of magnitude) by laser patterning. The behavior is opposite for the bilayer $ReS_2$, which is noncentrosymmetric in the unpatterned form. Upon laser patterning, the bilayer switched to the centrosymmetric 2H phase and the SHG signal was correspondingly reduced (also ∼2 orders of magnitude). This laser-induced 1T′-to-2H phase transition was monitored by polarization-resolved SHG measurements, which is a powerful method to directly visualize changes in a crystal structure. We showed that the observed laser-induced phase transition was reversible and the healing process could be sped up by heat. The reversed process was also investigated by polarization-resolved SHG, and the symmetry profiles were obtained for each healing steps. It is widely accepted, that the optical and electronic properties of TMD materials are very important for a broad range of applications.[49] In this work we showed that an active control of these properties is possible by reversible and highly nonlinear laser patterning of $ReS_2$. More generally, these results offer new ways for active manipulation of 2D materials and their heterostructures by light.

## METHODS

**Sample Preparation.** Samples were prepared on a thin microscope glass (170 μm) coverslips. The glass coverslips were cleaned in acetone and isopropanol at 60 °C in an ultrasonicator, dried by a stream of compressed nitrogen, and followed by oxygen plasma cleaning. Mono- and few-layer $ReS_2$ flakes were mechanically exfoliated from bulk crystals (HQ-graphene) onto polydimethylsiloxane (PDMS) stamps using the scotch-tape method and then transferred onto clean glass substrates using the all-dry transfer method.[50] The thicknesses of transferred $ReS_2$ flakes were determined using scanning probe microscopy (SPM, Bruker Dimension 3100).

**Raman Spectroscopy.** Raman spectra were collected in a backscattering geometry using a commercial Raman microscope (WITec alpha300R), equipped with a 100× air objective (NA = 0.9), under a $\lambda_{exc}$ = 532 nm continuous-wave laser excitation. Optical bright-field images were recorded using the same commercial microscope setup.

**SHG Measurements.** SHG measurements were performed using a home-built microscope coupled to a tunable (690−1040 nm) Ti:sapphire femtosecond laser (MaiTai HP-Newport Spectra-Physics) with a ∼100 fs pulse duration and 80 MHz repetition rate as shown in Figure 1a. The excitation wavelength was set to 1040 nm, which provides optimal conditions for SHG of $ReS_2$. The fundamental laser beam was directed to the sample by passing through a dichroic mirror (Semrock, FF775-Di01-25 × 36), broadband linear polarizer (Thorlabs, WP25M-UB) and $\lambda/2$ wave plate (Thorlabs, SAHWP05M-700), respectively. Then, the beam was focused


https://doi.org/10.1021/acsphotonics.1c01358
ACS Photonics 2022, 9, 518−526

on the sample mounted on the piezo stage (Mad City Laboratories, Nano-LP200) using a 40× microscope objective (Nikon, NA = 0.95) with a spherical aberration correction ring to reduce the deterioration of the image due to the finite cover glass thickness. The SHG signal was collected following the same optical path and separated from the fundamental beam by a dichroic mirror and a short pass filter (Semrock, FF01-720/SP-25). The signal was then focused onto the entrance of a 50 $\mu$m multimode fiber coupled to either a spectrometer (Andor 500i, equipped with Newton 920 CCD camera) or an avalanche photodiode (APD, IDQ, ID100 Visible Single-Photon Detector) in order to perform the SHG mapping. The piezo stage was set to the 0.4 nm accuracy in the steps and SHG counts were detected by the avalanche photodiode (APD). For polarization-dependent SHG measurements, the linear polarizer was fixed to the polarization of the incident laser and the $\lambda/2$ wave plate was rotated by 5° every step (every step, thus, rotated the polarization of the fundamental beam by 10°). For each polarization, a spatial SHG mapping was performed. The images were then analyzed to obtain the polarization-resolved SHG data.

## ■ ASSOCIATED CONTENT

### Supporting Information

The Supporting Information is available free of charge at https://pubs.acs.org/doi/10.1021/acsphotonics.1c01358.

Experimental details, data analysis methods, and fitting of the experimental data for all SHG polarization-resolved measurements (PDF)

## ■ AUTHOR INFORMATION


### Corresponding Author

**Timur O. Shegai** − *Department of Physics, Chalmers University of Technology, 412 96 Göteborg, Sweden;* orcid.org/0000-0002-4266-3721; Email: timurs@chalmers.se

### Authors

**Betül Küçüköz** − *Department of Physics, Chalmers University of Technology, 412 96 Göteborg, Sweden*

**Battulga Munkhbat** − *Department of Physics, Chalmers University of Technology, 412 96 Göteborg, Sweden*

Complete contact information is available at: https://pubs.acs.org/10.1021/acsphotonics.1c01358



### Funding

The authors acknowledge financial support from the Swedish Research Council (under VR Miljö project, grant no: 2016-06059), Knut and Alice Wallenberg Foundation (project no: 2019.0140), Chalmers Excellence Initiative Nano and 2D-TECH VINNOVA competence center (ref. 2019-00068).


### Notes

The authors declare no competing financial interest.

## ■ ACKNOWLEDGMENTS

The authors acknowledge fruitful discussions with Denis G. Baranov, Michael Stührenberg, Andrew B. Yankovich, Tomasz J. Antosiewicz, Joakim Andréasson, and Eva Olsson.

## ■ REFERENCES


(1) Rodin, A. In *2D Semiconductor Material Devices*; Chi, D., Goh, K. J, Wee, A. T., Eds.; Materials Today; Elsevier, 2020; pp 1−23.

(2) Yu, P.; et al. Metal−Semiconductor Phase-Transition in WSe2(1-x)Te2x Monolayer. *Adv. Mater.* **2017**, *29*, 1603991.

(3) Ma, Y.; Liu, B.; Zhang, A.; Chen, L.; Fathi, M.; Shen, C.; Abbas, A. N.; Ge, M.; Mecklenburg, M.; Zhou, C. Reversible Semiconducting-to-Metallic Phase Transition in Chemical Vapor Deposition Grown Monolayer WSe2 and Applications for Devices. *ACS Nano* **2015**, *9*, 7383−7391.

(4) Duerloo, K.-A. N.; Li, Y.; Reed, E. J. Structural phase transitions in two-dimensional Mo- and W-dichalcogenide monolayers. *Nat. Commun.* **2014**, *5*, 4214.

(5) Malard, L. M.; Alencar, T. V.; Barboza, A. P. M.; Mak, K. F.; De Paula, A. M. Observation of intense second harmonic generation from MoS2 atomic crystals. *Phys. Rev. B* **2013**, *87*, 201401.

(6) Kumar, N.; Najmaei, S.; Cui, Q.; Ceballos, F.; Ajayan, P. M.; Lou, J.; Zhao, H. Second harmonic microscopy of monolayer MoS2. *Phys. Rev. B* **2013**, *87*, 161403.

(7) Wang, G.; Marie, X.; Gerber, I.; Amand, T.; Lagarde, D.; Bouet, L.; Vidal, M.; Balocchi, A.; Urbaszek, B. Giant enhancement of the optical second-harmonic emission of WSe 2 monolayers by laser excitation at exciton resonances. *Phys. Rev. Lett.* **2015**, *114*, 097403.

(8) Fryett, T.; Zhan, A.; Majumdar, A. Cavity nonlinear optics with layered materials. *Nanophotonics* **2017**, *7*, 355−370.

(9) Fryett, T. K.; Seyler, K. L.; Zheng, J.; Liu, C.-H.; Xu, X.; Majumdar, A. Silicon photonic crystal cavity enhanced second-harmonic generation from monolayer WSe 2. *2D Mater.* **2017**, *4*, 015031.

(10) Chen, H.; Corboliou, V.; Solntsev, A. S.; Choi, D.-Y.; Vincenti, M. A.; de Ceglia, D.; de Angelis, C.; Lu, Y.; Neshev, D. N. Enhanced second-harmonic generation from two-dimensional MoSe2 on a silicon waveguide. *Light: Sci. Appl.* **2017**, *6*, e17060.

(11) Bernhardt, N.; Koshelev, K.; White, S. J.; Meng, K. W. C.; Fröch, J. E.; Kim, S.; Tran, T. T.; Choi, D.-Y.; Kivshar, Y.; Solntsev, A. S. Quasi-BIC Resonant Enhancement of Second-Harmonic Generation in WS2Monolayers. *Nano Lett.* **2020**, *20*, 5309−5314.

(12) Liu, F.; Wu, W.; Bai, Y.; Chae, S. H.; Li, Q.; Wang, J.; Hone, J.; Zhu, X.-Y. Disassembling 2D van der Waals crystals into macroscopic monolayers and reassembling into artificial lattices. *Science* **2020**, *367*, 903−906.

(13) Koshelev, K.; Kruk, S.; Melik-Gaykazyan, E.; Choi, J.-H.; Bogdanov, A.; Park, H.-G.; Kivshar, Y. Subwavelength dielectric resonators for nonlinear nanophotonics. *Science* **2020**, *367*, 288−292.

(14) Yin, X.; Ye, Z.; Chenet, D. A.; Ye, Y.; O'Brien, K.; Hone, J. C.; Zhang, X. Edge Nonlinear Optics on a $MoS_2$ Atomic Monolayer. *Science* **2014**, *344*, 488−490.

(15) Busschaert, S.; Reimann, R.; Cavigelli, M.; Khelifa, R.; Jain, A.; Novotny, L. Transition Metal Dichalcogenide Resonators for Second Harmonic Signal Enhancement. *ACS Photonics* **2020**, *7*, 2482.

(16) Munkhbat, B.; Yankovich, A. B.; Baranov, D. G.; Verre, R.; Olsson, E.; Shegai, T. O. Transition metal dichalcogenide metamaterials with atomic precision. *Nat. Commun.* **2020**, *11*, 4604.

(17) Castellanos-Gomez, A.; Roldán, R.; Cappelluti, E.; Buscema, M.; Guinea, F.; van der Zant, H. S. J.; Steele, G. A. Local Strain Engineering in Atomically Thin MoS2. *Nano Lett.* **2013**, *13*, 5361−5366.

(18) Roldán, R.; Castellanos-Gomez, A.; Cappelluti, E.; Guinea, F. Strain engineering in semiconducting two-dimensional crystals. *J. Phys.: Condens. Matter* **2015**, *27*, 313201.

(19) Li, D.; Wei, C.; Song, J.; Huang, X.; Wang, F.; Liu, K.; Xiong, W.; Hong, X.; Cui, B.; Feng, A.; Jiang, L.; Lu, Y. Anisotropic Enhancement of Second-Harmonic Generation in Monolayer and Bilayer MoS2 by Integrating with TiO2 Nanowires. *Nano Lett.* **2019**, *19*, 4195−4204.

(20) Wu, W.; Wang, L.; Li, Y.; Zhang, F.; Lin, L.; Niu, S.; Chenet, D.; Zhang, X.; Hao, Y.; Heinz, T. F.; Hone, J.; Wang, Z. L. Piezoelectricity of single-atomic-layer MoS2 for energy conversion and piezotronics. *Nature* **2014**, *514*, 470−474.

(21) Mennel, L.; Furchi, M. M.; Wachter, S.; Paur, M.; Polyushkin, D. K.; Mueller, T. Optical imaging of strain in two-dimensional crystals. *Nat. Commun.* **2018**, *9*, 1−6.

(22) Liang, J.; et al. Monitoring Local Strain Vector in Atomic-Layered MoSe2 by Second-Harmonic Generation. *Nano Lett.* **2017**, *17*, 7539−7543.
(23) Wu, W.; Wang, L.; Li, Y.; Zhang, F.; Lin, L.; Niu, S.; Chenet, D.; Zhang, X.; Hao, Y.; Heinz, T. F.; et al. Piezoelectricity of single-atomic-layer MoS2 for energy conversion and piezotronics. *Nature* **2014**, *514*, 470−474.
(24) Song, Y.; Hu, S.; Lin, M.-L.; Gan, X.; Tan, P.-H.; Zhao, J. Extraordinary Second Harmonic Generation in ReS2 Atomic Crystals. *ACS Photonics* **2018**, *5*, 3485−3491.
(25) Tongay, S.; et al. Monolayer behaviour in bulk ReS2 due to electronic and vibrational decoupling. *Nat. Commun.* **2014**, *5*, 3252.
(26) Chenet, D. A.; Aslan, O. B.; Huang, P. Y.; Fan, C.; van der Zande, A. M.; Heinz, T. F.; Hone, J. C. In-Plane Anisotropy in Mono- and Few-Layer ReS2 Probed by Raman Spectroscopy and Scanning Transmission Electron Microscopy. *Nano Lett.* **2015**, *15*, 5667.
(27) Zhang, Q.; Fu, L. Novel Insights and Perspectives into Weakly Coupled $ReS_2$ toward Emerging Applications. *Chem.* **2019**, *5*, 505−525.
(28) Zhou, D.; Zhou, Y.; Pu, C.; Chen, X.; Lu, P.; Wang, X.; An, C.; Zhou, Y.; Miao, F.; Ho, C.-H.; Sun, J.; Yang, Z.; Xing, D. Pressure-induced metallization and superconducting phase in ReS2. *npj Quantum Mater.* **2017**, *2*, 1−7.
(29) Gogna, R.; Zhang, L.; Deng, H. Self-Hybridized, Polarized Polaritons in ReS2 Crystals. *ACS Photonics* **2020**, *7*, 3328−3332.
(30) Qiao, X.-F.; Wu, J.-B.; Zhou, L.; Qiao, J.; Shi, W.; Chen, T.; Zhang, X.; Zhang, J.; Ji, W.; Tan, P.-H. Polytypism and unexpected strong interlayer coupling in two-dimensional layered ReS2. *Nanoscale* **2016**, *8*, 8324−8332.
(31) He, R.; Yan, J.-A.; Yin, Z.; Ye, Z.; Ye, G.; Cheng, J.; Li, J.; Lui, C. H. Coupling and Stacking Order of ReS2 Atomic Layers Revealed by Ultralow-Frequency Raman Spectroscopy. *Nano Lett.* **2016**, *16*, 1404.
(32) Lorchat, E.; Froehlicher, G.; Berciaud, S. Splitting of Interlayer Shear Modes and Photon Energy Dependent Anisotropic Raman Response in N-Layer ReSe2 and ReS2. *ACS Nano* **2016**, *10*, 2752.
(33) Rahman, M.; Davey, K.; Qiao, S.-Z. Advent of 2D Rhenium Disulfide (ReS2): Fundamentals to Applications. *Adv. Funct. Mater.* **2017**, *27*, 1606129.
(34) Zhou, Y.; Maity, N.; Rai, A.; Juneja, R.; Meng, X.; Roy, A.; Zhang, Y.; Xu, X.; Lin, J.-F.; Banerjee, S. K.; Singh, A. K.; Wang, Y. Stacking-Order-Driven Optical Properties and Carrier Dynamics in $ReS_2$. *Adv. Mater.* **2020**, *32*, 1908311.
(35) Dhakal, K. P.; Kim, H.; Lee, S.; Kim, Y.; Lee, J.; Ahn, J.-H. Probing the upper band gap of atomic rhenium disulfide layers. *Light: Sci. Appl.* **2018**, *7*, 98.
(36) Cho, S.; Kim, S.; Kim, J. H.; Zhao, J.; Seok, J.; Keum, D. H.; Baik, J.; Choe, D.-H.; Chang, K. J.; Suenaga, K.; Kim, S. W.; Lee, Y. H.; Yang, H. Phase patterning for ohmic homojunction contact in $MoTe_2$. *Science* **2015**, *349*, 625−628.
(37) Tan, Y.; Luo, F.; Zhu, M.; Xu, X.; Ye, Y.; Li, B.; Wang, G.; Luo, W.; Zheng, X.; Wu, N.; Yu, Y.; Qin, S.; Zhang, X.-A. Controllable 2H-to-1T′ phase transition in few-layer $MoTe_2$. *Nanoscale* **2018**, *10*, 19964−19971.
(38) Song, Y.; Tian, R.; Yang, J.; Yin, R.; Zhao, J.; Gan, X. Second Harmonic Generation in Atomically Thin $MoTe_2$. *Adv. Opt. Mater.* **2018**, *6*, 1701334.
(39) Wang, M.; Li, D.; Liu, K.; Guo, Q.; Wang, S.; Li, X. Nonlinear Optical Imaging, Precise Layer Thinning, and Phase Engineering in $MoTe_2$ with Femtosecond Laser. *ACS Nano* **2020**, *14*, 11169−11177.
(40) Turunen, M. T.; Hulkko, E.; Mentel, K. K.; Bai, X.; Akkanen, S.-T.; Amini, M.; Li, S.; Lipsanen, H.; Pettersson, M.; Sun, Z. Deterministic Modification of CVD Grown Monolayer MoS2 with Optical Pulses. *Adv. Mater. Interfaces* **2021**, *8*, 2002119.
(41) Ma, Y.; Liu, B.; Zhang, A.; Chen, L.; Fathi, M.; Shen, C.; Abbas, A. N.; Ge, M.; Mecklenburg, M.; Zhou, C. Reversible Semiconducting-to-Metallic Phase Transition in Chemical Vapor Deposition Grown Monolayer WSe2 and Applications for Devices. *ACS Nano* **2015**, *9*, 7383−7391.
(42) Wang, R.; Yu, Y.; Zhou, S.; Li, H.; Wong, H.; Luo, Z.; Gan, L.; Zhai, T. Strategies on Phase Control in Transition Metal Dichalcogenides. *Adv. Funct. Mater.* **2018**, *28*, 1802473.
(43) Kappera, R.; Voiry, D.; Yalcin, S.; Branch, B.; Gupta, G.; Mohite, A. D.; Chhowalla, M. Phase-engineered low-resistance contacts for ultrathin MoS2 transistors. *Nat. Mater.* **2014**, *13*, 1128−1134.
(44) Huang, H. H.; Fan, X.; Singh, D. J.; Zheng, W. T. Recent progress of TMD nanomaterials: phase transitions and applications. *Nanoscale* **2020**, *12*, 1247−1268.
(45) Boyd, R. W. In *Nonlinear Opt.*, third ed.; Boyd, R. W., Ed.; Academic Press: Burlington, 2008; pp 1−67.
(46) Wen, X.; Gong, Z.; Li, D. Nonlinear optics of two-dimensional transition metal dichalcogenides. *InfoMat* **2019**, *1*, 317−337.
(47) Lim, C.-K.; Li, X.; Li, Y.; Drew, K. L. M.; Palafox-Hernandez, J. P.; Tang, Z.; Baev, A.; Kuzmin, A. N.; Knecht, M. R.; Walsh, T. R.; Swihart, M. T.; Ågren, H.; Prasad, P. N. Plasmon-enhanced two-photon-induced isomerization for highly-localized light-based actuation of inorganic/organic interfaces. *Nanoscale* **2016**, *8*, 4194−4202.
(48) Roy, P.; Sardjan, A. S.; Cnossen, A.; Browne, W. R.; Feringa, B. L.; Meech, S. R. Excited State Structure Correlates with Efficient Photoconversion in Unidirectional Motors. *J. Phys. Chem. Lett.* **2021**, *12*, 3367−3372.
(49) Mak, K. F.; Shan, J. Photonics and optoelectronics of 2D semiconductor transition metal dichalcogenides. *Nat. Photonics* **2016**, *10*, 216−226.
(50) Castellanos-Gomez, A.; Buscema, M.; Molenaar, R.; Singh, V.; Janssen, L.; van der Zant, H. S. J.; Steele, G. A. Deterministic transfer of two-dimensional materials by all-dry viscoelastic stamping. *2D Mater.* **2014**, *1*, 011002.

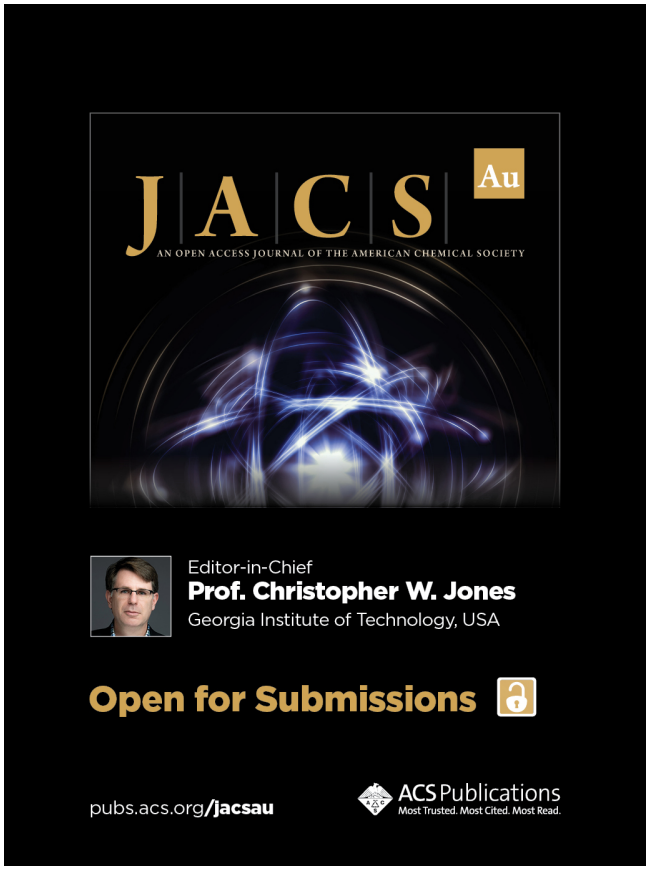



https://doi.org/10.1021/acsphotonics.1c01358
ACS Photonics 2022, 9, 518−526